

# Geo-feature modeling uncertainties in discrete global grids: a case study of downtown Calgary, Canada

Mingke Li and Emmanuel Stefanakis

**Abstract:** The Open Geospatial Consortium has officially adopted discrete global grid systems (DGGS) as a new option for Earth reference standards. Many state-of-the-art DGGS implementations have been developed, revealing the potential for DGGS applications. Before the wide application of DGGS in solving real-world problems, however, the potential uncertainties of modeling on DGGS should be investigated and documented. This study focused on the uncertainties of geo-feature modeling on DGGS, quantitatively measured the point position displacement and line and polygon features' geometry distortion, and evaluated the validity of topological relationships. Specifically, traffic cameras (points), main streets (lines), and land-cover classes (polygons) of downtown Calgary (AB, Canada) were modeled in various DGGS configurations at multiple resolutions. Results showed that the point displacement and polygon distortion generally reduced when being modeled at a higher resolution. The tessellations with the monotonical convergence characteristic are recommended if cell indices are expected to represent levels of model precision. Line features' fidelity was affected by grid tessellations, resolution levels, grid orientation relative to the Earth, and the rotated line directions. The degree of the line distortion was not straightforward to forecast. Maintaining the topological validity between spatial objects with various granularities was challenging and needed further algorithm development for DGGS implementations. The study outcomes can serve as useful guidelines in the selection among grid types, refinement ratios, and resolution levels when applying DGGS implementations to urban environments. This paper also pinpoints several research directions that can benefit the quantization and analysis of vector features on DGGS.

**Key words:** discrete global grid systems, Open Geospatial Consortium, geo-feature modeling, geometric uncertainties, topological uncertainties.

**Résumé :** L'Open Geospatial Consortium a officiellement adopté les Systèmes de grilles mondiaux discrets (DGGS — « discrete global grid systems ») comme nouvelle option pour les normes de référence terrestre. Plusieurs mises en place d'avant-garde des DGGS ont été développées, révélant le potentiel des applications des DGGS. Toutefois, avant d'en arriver à une application étendue des DGGS pour régler les problèmes du monde réel, les incertitudes potentielles de la modélisation des DGGS devraient être examinées et documentées. La présente étude met l'accent sur les incertitudes de la modélisation des caractéristiques géographiques des DGGS, ayant mesuré quantitativement le déplacement de la position du point ainsi que la distorsion géographique des caractéristiques des lignes et des polygones et ayant évalué la validité des relations topologiques. Plus particulièrement, les caméras de circulation (points), les rues principales (lignes) et les catégories de couverture terrestre (polygones) du centre-ville de Calgary ont été modélisées dans diverses

Received 13 April 2020. Accepted 25 September 2020.

**M. Li and E. Stefanakis.** Department of Geomatics Engineering, Schulich School of Engineering, University of Calgary, 2500 University Drive NW, Calgary, AB T2N 1N4, Canada.

**Corresponding author:** Mingke Li (email: [mingke.li@ucalgary.ca](mailto:mingke.li@ucalgary.ca)).

Copyright remains with the author(s) or their institution(s). Permission for reuse (free in most cases) can be obtained from [copyright.com](http://copyright.com).

configurations des DGGS à de multiples résolutions. Les résultats ont permis de déterminer que le déplacement du point et la distortion du polygone diminuent généralement lorsqu'ils sont modélisés à une résolution plus élevée. Les pavages avec la caractéristique de la convergence monotone sont recommandés si on s'attend à ce que les indices des cellules représentent les niveaux de précision du modèle. La fidélité de la caractéristique de la ligne a été altérée par les pavages de la grille, les niveaux de résolution, l'orientation de la grille par rapport à la terre et le sens de la rotation de la ligne. Le degré de distortion de la ligne n'était pas facile à prévoir. Le maintien de la validité topologique entre les objets spatiaux avec diverses granularités était complexe et nécessitait le développement d'un autre algorithme pour les mises en place des DGGS. Les résultats de l'étude peuvent servir de lignes directrices utiles dans la sélection parmi les types de grilles, les ratios d'amélioration et les niveaux de résolution lors de l'application des mises en place des DGGS aux environnements urbains. La présente communication identifie également plusieurs orientations de recherche qui peuvent tirer profit de la quantification et de l'analyse des caractéristiques des vecteurs sur les DGGS. [Traduit par la Rédaction]

**Mots-clés :** Systèmes de grilles mondiaux discrets, Open Geospatial Consortium, modélisation des caractéristiques géographiques, modélisation des caractéristiques géographiques, incertitudes géométriques, incertitudes topologiques.

## Introduction

Geographical information is characterized by spatial heterogeneity, spatial dependence, and vagueness (Ahlgren et al. 2000). Uncertainty exists in the whole geographical process such as geographical abstraction, data acquisition, data processing, and application (Zhang and Goodchild 2002). Spatial data modeling is a typical geographical abstraction process to convert the geographical reality to a form that can be stored and conveyed digitally (Goodchild 1989). The inevitable differences between the geographical reality and the modeled data result in uncertainties, including the inaccuracy of geographical position, attributes, and spatial relationships (Roberts and Robertson 2016). Uncertainty can also exist in transforming data models even if the data stored in the initial model are free of error (Zhang and Goodchild 2002). Vector and raster, as typical spatial data models, have long been used to store, manage, and present spatial information. A vector data model represents real-world objects by coordinates using three basic feature types: point, line, and polygon. A raster data model is made of regularly spaced grid cells attached with values. Methods of vectorization and rasterization have been studied previously to reach more accuracy and higher efficiency (e.g., Lee et al. 2000; Wang et al. 2013).

During the long period of geographic information systems (GIS) development, spatial data models reference spatial information to the continuous space with coordinate reference systems; however, a continuous reference space suffers from some limitations compared with a discrete reference system. For example, an areal unit in a discrete system can moderate uncertainties around a geographic location, while a dimensionless point used as the basic unit in the continuous space cannot. Besides, a point-based coordinate system is not practical to successively observe a phenomenon at the same location while a discrete space consisting of areal cells has the potential of continuous observations.

With the advance of the theoretical and technological development, discrete global grid systems (DGGS) have been recognized as a new spatial reference system based on discrete cells, addressing the above limitations of the continuous reference space (Mahdavi-Amiri et al. 2015b; Alderson et al. 2020). In short, a DGGS is a system of hierarchical discrete global grids (DGG) where the DGG at each resolution tessellate the entire Earth's surface by uniform cells without any overlaps and assign a single identifier to each cell (OGC 2017). In 2017, the Open Geospatial Consortium (OGC) officially adopted DGGS as a new reference standard and codified the qualities of compliant DGGS implementations that support the

interoperability and development flexibility ([OGC 2017](#)). Other than the advantages as a discrete reference space, a DGGS is advantageous compared with the traditional GIS from at least five other aspects. (i) DGGS can serve as a uniform data model to standardize geospatial information from various data sources and be independent of the original data formats, which facilitates the multi-source data management ([Peterson 2016](#)). (ii) DGGS cell locations are fixed at a certain resolution level and the spatial data associated with a cell are aligned, so that location-based data queries can be accelerated given that spatial information is stored in a “congruent geography” instead of the sliced theme layers ([Goodchild 2018](#)). (iii) Multi-scale analysis can benefit from the hierarchical nature of DGGS because it uses a hierarchical tessellation of cells to partition and address the globe where resolutions are inherently defined by the cell indices ([Goodchild and Yang 1989](#)). (iv) DGGS can help to achieve a better analysis accuracy because the Earth’s curvature is considered when constructing a DGGS, and the spatial resolution at each level is consistent given the nearly unified cell size ([Alderson et al. 2020](#)). All parts of the Earth’s surface, including the polar regions which would need special projections during the previous research, will be treated consistently and fairly. (v) DGGS provide aggregation units of nearly uniform size and shape and can convey the information without a visual deformation of the content when being displayed.

The last few decades have witnessed the development of DGGS technologies, including various system configurations (e.g., [Mahdavi-Amiri et al. 2013; Sahr et al. 2015; Gibb 2016](#)), cell indexing mechanisms (e.g., [Mocnik 2018; Tong et al. 2019; Uher et al. 2019](#)), interoperability functions (e.g., [Mahdavi-Amiri et al. 2015a, 2016](#)), and data representation methods on DGGS (e.g., [Stough et al. 2014; Mahdavi-Amiri et al. 2018](#)). Four indexing mechanisms are most used in DGGS implementations, including the hierarchy-based, space-filling curve-based, coordinate-based, and encoded address schemas ([Mahdavi-Amiri et al. 2015b](#)). Additionally, some state-of-the-art DGGS implementations have been proposed that revealed the potential for DGGS applications in different subject areas and various purposes. To name just a few, current open-source DGGS implementations include H3, OpenEAGGR, DGGRID, HEALPix, rHEALPix, and geogrid ([OpenEAGGR 2017; Uber 2017; JPL 2018; Bowater and Stefanakis 2019; Mocnik 2019; Sahr 2020](#)). Particularly, the C++ library DGGRID has the R binding library dggridR and the Python binding library pydggrid and allows users to customize a DGGS by defining the cell shape, refinement ratio, orientation of the grid relative to the Earth surface, and polyhedral projection method. Compared with other open-source libraries including H3, OpenEAGGR, and S2, dggridR was found to have the highest scalability to handle large datasets ([Bondaruk et al. 2020](#)).

Although DGGS have demonstrated both theory and implementation development, they have not been applied widely to support real-world data management, analysis, or decision-making. Before wide application, the potential uncertainties of modeling on a DGGS should be fully investigated. Uncertainties can occur during the quantization process, namely assigning and retrieving data values to and from DGGS cells, and lead to further misinformation and inappropriate decision-making. The uncertainties mainly include the errors of spatial objects’ position, geometric characteristics, attributes, and topological relationships. This should be more of a concern in the case of urban applications due to the complicated spatial entities.

This paper quantitatively evaluated the uncertainties of geo-feature modeling on DGGS in the urban region, including the measure of point position displacement and line and polygon features’ geometry fidelity, and the evaluation of the violated topological relationships. The remainder of the paper is organized as follows. The next section presents the methodology used, including the study area and data sources, data modeling on DGGS, and the uncertainty analysis of geometry and topology. The third section presents and discusses the

results of the uncertainty analysis regarding both geometry and topology. Finally, general conclusions and future research directions are summarized in the last section.

## Methodology

### Study area and data sources

This research used the downtown area in Calgary, AB, Canada, as a case study, and analyzed traffic cameras as points, main streets as lines, and land cover classification as polygons. The spatial information and attributes of these analysis objects were open-source vector data extracted from Open Calgary, the City of Calgary's open data portal, with the WGS84 datum and in the shapefile format ([OpenCalgary 2020](#)). The downtown area covered about 280.9 ha, and there were a total of 17 traffic cameras, 40 main streets, and 1122 land cover blocks (greater than  $1 \text{ m}^2$ ) included in the analysis ([Fig. 1](#)). The original 217 street segments from the obtained dataset were dissolved by street names in the data cleansing process. Geodesic length or area of all streets or blocks were calculated based on the WGS84 datum: street segment length ranged from 43.8 to 2251.4 m,  $\bar{x} = 550.1 \text{ m}$ , and  $\sigma = 563.1 \text{ m}$ ; block area ranged from 1.4 to 135382.5  $\text{m}^2$ ,  $\bar{x} = 2503.3 \text{ m}^2$ , and  $\sigma = 7949.4 \text{ m}^2$ .

### Modeling of vector features on DGGS

Vector datasets were modeled on DGGS using the open-source R library dggridR which generates icosahedral DGGS and enables users to define the cell shapes, refinement ratio, projection methods, the orientation of the base polyhedron relative to the Earth, and resolution levels ([Barnes 2016](#)). To understand the impacts of various configurations, four tessellations were tested in this study: (i) Icosahedral Snyder Equal Area Aperture 3 Hexagonal Grid (ISEA3H), (ii) Icosahedral Snyder Equal Area Aperture 4 Hexagonal Grid (ISEA4H), (iii) Icosahedral Snyder Equal Area Aperture 4 Triangular Grid (ISEA4T), and (iv) Icosahedral Snyder Equal Area Aperture 4 Diamond Grid (ISEA4D). To evaluate the effects from different granularities, grids at successive resolution levels were generated for each of the above four tessellations. The default orientation of the base polyhedron relative to the Earth was used, where the grids are symmetrical about the equator and merely one vertex of the icosahedron falls on land. The parameters of the default orientation are latitude of the pole ( $\lambda$ ) = 58.2825°, longitude of the pole ( $\varphi$ ) = 11.2500°, and azimuth ( $\alpha$ ) = 0°. The analysis was carried out using R version 3.6.2 ([R Core Team 2020](#)), and the results were visualized by ArcGIS Pro 2.4 (ESRI, Redlands, CA, USA).

When modeling spatial points on DGGS, original points were converted to the individual cells that they fell in. Each cell has a unique identifier at each resolution, and the position of the cell centroid represents the cell's geographical coordinates ([Fig. 2a](#)). Line features were converted as a sequence of DGGS cells where the original lines intersect ([Fig. 2b](#)). Polygons were modeled as a collection of DGGS cells where only the intersected polygon with dominant area proportions was assigned to the target cell. As illustrated in [Fig. 2c](#), cell A and cell B were covered by more than one original polygon, and the cells were determined as "Building/Paved" and "Roads/Rail lines", respectively, depending on which intersected polygon had a higher intersected area. Other quantization methods for modeling polygons include assigning each of the intersected polygons' attributes to the same DGGS cell. Nonetheless, the methods used in this study ensured that each cell only represented one land cover class, so that potential duplicated area calculation and topological violation can be avoided.

### Uncertainty analysis of geometry

For the analysis regarding points, the uncertainty was quantitatively measured as the displacement, which was the WGS84-based geodesic distances between the geographical

**Figure 1.** Traffic cameras, main streets, and land cover classes in the downtown area of Calgary, AB, Canada. The data were obtained from the Open Calgary ([OpenCalgary 2020](#)) and visualized in ArcGIS Pro 2.4 with the “World Topographic Map” as the base map ([Esri 2020](#)). [Colour online.]

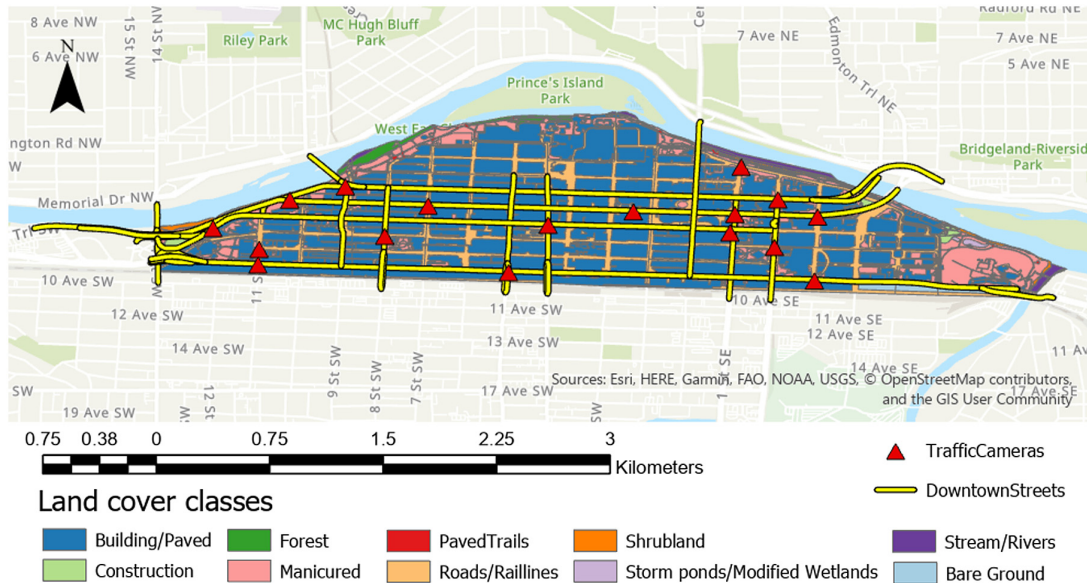


**Figure 2.** Illustration of the geo-feature modeling and measuring processes: (a) convert a point object to a hexagonal cell with the cell centroid as the referencing point; (b) convert a line feature to a set of hexagonal cells and measure the line length as the sum of the distances between the cell centroids; (c) overlay a hexagonal grid system on the target polygons and determine the grid attributes by the dominant area. The grids and cell centroids were created via the dggridR library ([Barnes 2016](#)) and visualized in ArcGIS Pro 2.4 with the “World Topographic Map” as the base map ([Esri 2020](#)). [Colour online.]

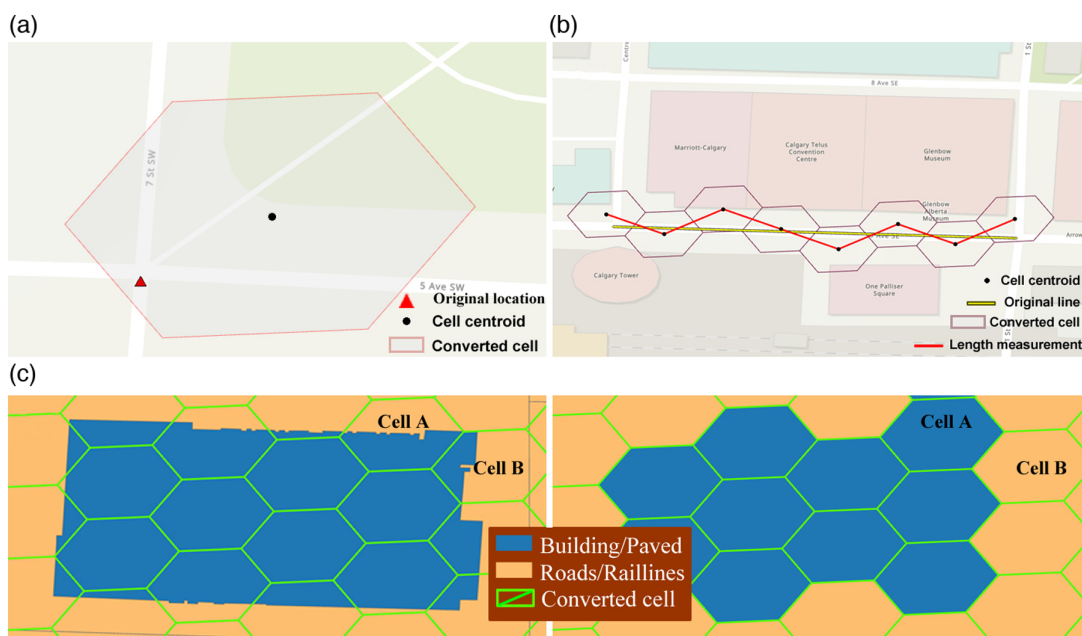


**Table 1.** Quantitative information of the configurations at various resolution levels tested in this study.

Configuration	Resolution level	Cell area ( $\text{m}^2$ )	Spacing (m)	CLS (m)
ISEA3H	24	180.60	13.27	15.16
	25	60.20	7.66	8.75
	26	20.07	4.42	5.05
	27	6.67	2.55	2.92
	28	2.23	1.47	1.68
ISEA4H	18	742.24	26.91	30.74
	19	185.56	13.45	15.37
	20	46.39	6.73	7.69
	21	11.60	3.36	3.84
	22	2.90	1.68	1.92
ISEA4T	17	1484.49	31.07	43.48
	18	371.12	15.54	21.74
	19	92.78	7.77	10.87
	20	23.20	3.88	5.43
	21	5.80	1.94	2.72
ISEA4D	18	742.24	26.91	30.74
	19	185.56	13.45	15.37
	20	46.39	6.73	7.69
	21	11.60	3.36	3.84
	22	2.90	1.68	1.92

Note: ISEA3H, Icosahedral Snyder Equal Area Aperture 3 Hexagonal Grid; ISEA4H, Icosahedral Snyder Equal Area Aperture 4 Hexagonal Grid; ISEA4T, Icosahedral Snyder Equal Area Aperture 4 Triangular Grid; ISEA4D, Icosahedral Snyder Equal Area Aperture 4 Diamond Grid; CLS, the diameter of a spherical cap of the same area as a cell of the specified resolution.

coordinates of the original point and the geographical coordinates of the converted cell centroid. In this paper, points were modeled and displacements were calculated at 10 successive resolution levels from 21 to 30 for each of four DGGS configurations: ISEA3H, ISEA4H, ISEA4T, and ISEA4D.

For the analysis related to lines and polygons, four grid configurations including ISEA3H, ISEA4H, ISEA4T, and ISEA4D were generated at five successive resolution levels. Specifically, ISEA3H was tested at levels 24–28, ISEA4T was tested at levels 17–21, and ISEA4H and ISEA4D were tested at levels 18–22. The spacing between the cell centroids was about 2 m at the finest resolution levels for four configurations. The quantitative information of these configurations with tested resolution levels is summarized in Table 1. For modeled line features, the total segment distance between the DGGS cell centroids was calculated for each line (Fig. 2b). The difference between the original length and the total inter-centroid distance was viewed as an indicator of the preserved fidelity of the modeled line features. One of the streets was selected as an example to fully explore the influence of the rotation of the line feature and the orientation of the grid system relative to the Earth. Specifically, three orientation options were tested. (i) The grid is symmetrical about the equator and has one icosahedral vertex falling on land (default in the library dggridR), where  $\lambda = 58.2825^\circ$ ,  $\varphi = 11.2500^\circ$ , and  $\alpha = 0^\circ$  (Sahr et al. 2003). (ii) 12 icosahedral vertices locate in the ocean, where  $\lambda = 2.3009^\circ$ ,  $\varphi = -5.2454^\circ$ , and  $\alpha = 7.4666^\circ$  (Fuller and Applewhite 1975). (iii) The boundary of Canada is centered on a single face of the icosahedron, where  $\lambda = 37.6895^\circ$ ,  $\varphi = -51.6218^\circ$ , and  $\alpha = -72.6482^\circ$  (J. Zhou et al. 2020). The clockwise rotation of the line feature was tested at a  $15^\circ$  interval from  $0^\circ$  to  $345^\circ$ . The blocks' geodesic area were measured as the sum area of the DGGS cells (Fig. 2c). The difference between the original polygon area and the total cell area after being modeled on various DGGS configurations at multiple resolutions was calculated for each

polygon, that was then used to quantitatively measure the distortion of modeling areal objects on DGGS.

### Uncertainty analysis of topology

Topological relationships are commonly applied to three geometry types, i.e., point, line, and polygon. In this study, traffic cameras, main streets, and land cover classes were analyzed as points, lines, and polygons, respectively. There were typical topological relationships among these spatial objects: (i) traffic cameras were disjointed with each other; (ii) traffic cameras met streets; (iii) traffic cameras met or were inside of the “Roads/Rail lines” land cover class while disjointed with the other land cover classes; (iv) main street segments can meet, be disjoint, or intersect with each other; (v) main street segments were inside of or covered by the “Roads/Rail lines” land cover class while disjointed with the other land cover classes; and (vi) land cover classes met the adjacent ones at boundaries (Fig. 1). The above original topological relationships were evaluated with different DGGS configurations including ISEA3H, ISEA4H, ISEA4T, and ISEA4D, at five successive resolution levels as listed in Table 1.

## Results and discussion

### Geometric uncertainties

#### Points

Geodesic distances between the original points and the corresponding cell centroids were calculated for tessellations ISEA3H, ISEA4H, ISEA4T, and ISEA4D at resolution levels from 21 to 30. Results showed that the magnitude of the average displacement decreased with the finer resolutions on the grid ISEA3H, in which the average displacement was 0.19 m at the resolution level 30 (Fig. 3a). This result illustrated the monotonical convergence nature of the ISEA3H structure, where a parent cell’s vertices are its child cells’ centroids (Sahr et al. 2003). Consequently, a finer resolution leads to more precision when representing points on a DGGS (Fig. 4a). Global Grid Systems (previously known as PYXIS) adopted ISEA3H as their basic grid configuration considering this important characteristic (GGS 2019).

Different from ISEA3H, the average displacement on the tessellations ISEA4H, ISEA4T, and ISEA4D went through a decrease then an increase among the tested resolution levels with the level 26 or 27 as the changing point (Figs. 3b–3d). As illustrated in Fig. 4b, the grid ISEA4D lacks the monotonical convergence characteristic so that the displacement distances can diverge when transitioning to another resolution. In other words, an additional refinement does not necessarily provide more precision when representing a point on this grid tessellation. It should also be noted that the distance calculation may encounter the floating-point imprecision at the extremely high resolution, in which the computer memory does not have enough bits to distinguish geographic locations very close to each other and to calculate their distances. In this study, the smallest average position displacement was at resolution levels 26, 27, and 26 for tessellations ISEA4H, ISEA4T, and ISEA4D, with an average displacement of 0.04, 0.03, and 0.04 m, respectively (Figs. 3b–3d). The absolute displacement was greater on the grid ISEA3H compared with the other three grid tessellations at the same resolution because the cell size of ISEA3H was consistently larger among all the resolutions.

#### Polylines

Line features representing main streets in the downtown area have been converted to DGGS grids with different configurations at multiple resolutions (Fig. 5). Due to the discrete nature of DGGS, the meaning of the length of a line feature is different from that in a

**Figure 3.** Point displacement at resolution levels 21–30 with the tessellations of (a) Icosahedral Snyder Equal Area Aperture 3 Hexagonal Grid (ISEA3H), (b) Icosahedral Snyder Equal Area Aperture 4 Hexagonal Grid (ISEA4H), (c) Icosahedral Snyder Equal Area Aperture 4 Triangular Grid (ISEA4T), and (d) Icosahedral Snyder Equal Area Aperture 4 Diamond Grid (ISEA4D).

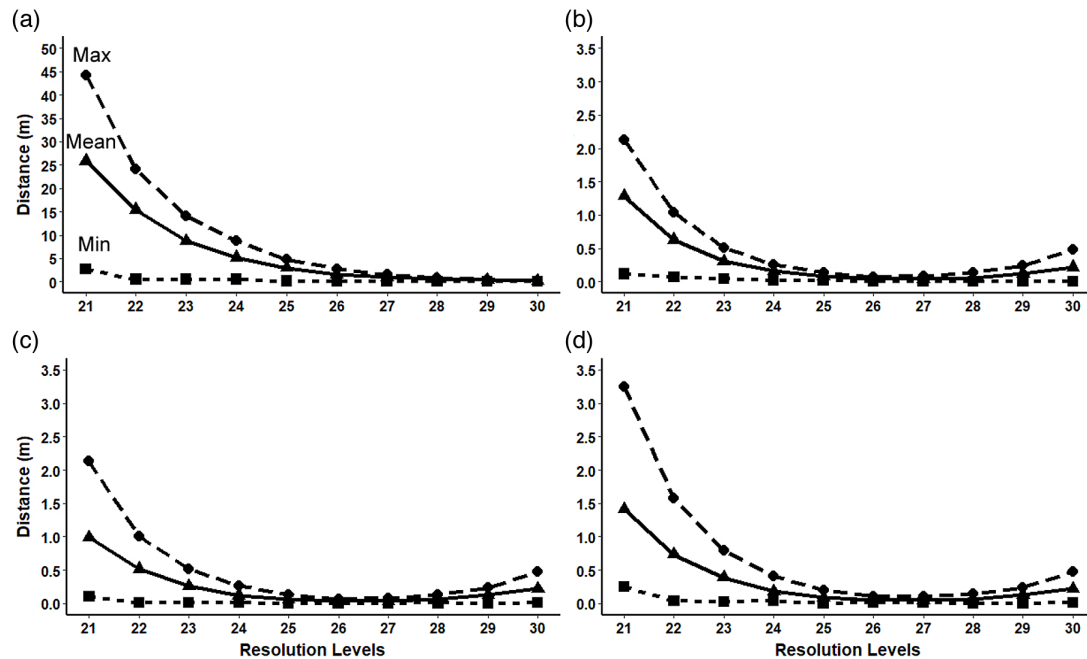


**Figure 4.** Illustration of distances between the original point and the centroids at three successively refined cells on the (a) hexagonal grids with aperture 3 which has the monotonical convergence nature ( $D_1 > D_2 > D_3$ ) and (b) diamond grids with aperture 4 which can lead to a diverged distance ( $D_2 > D_1 > D_3$ ). [Colour online.]

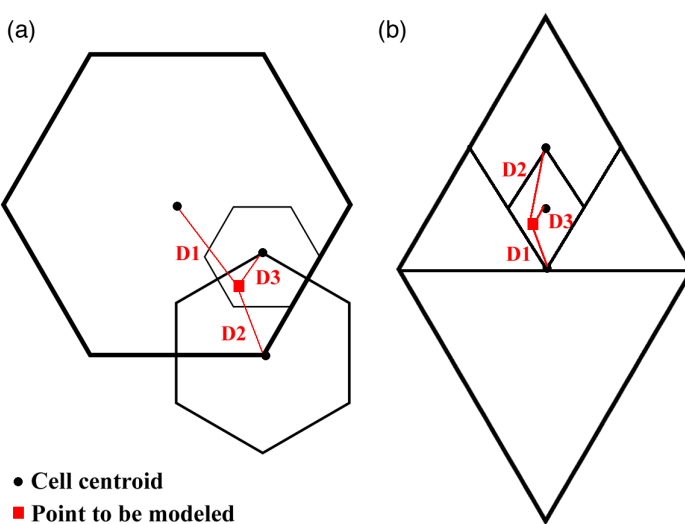
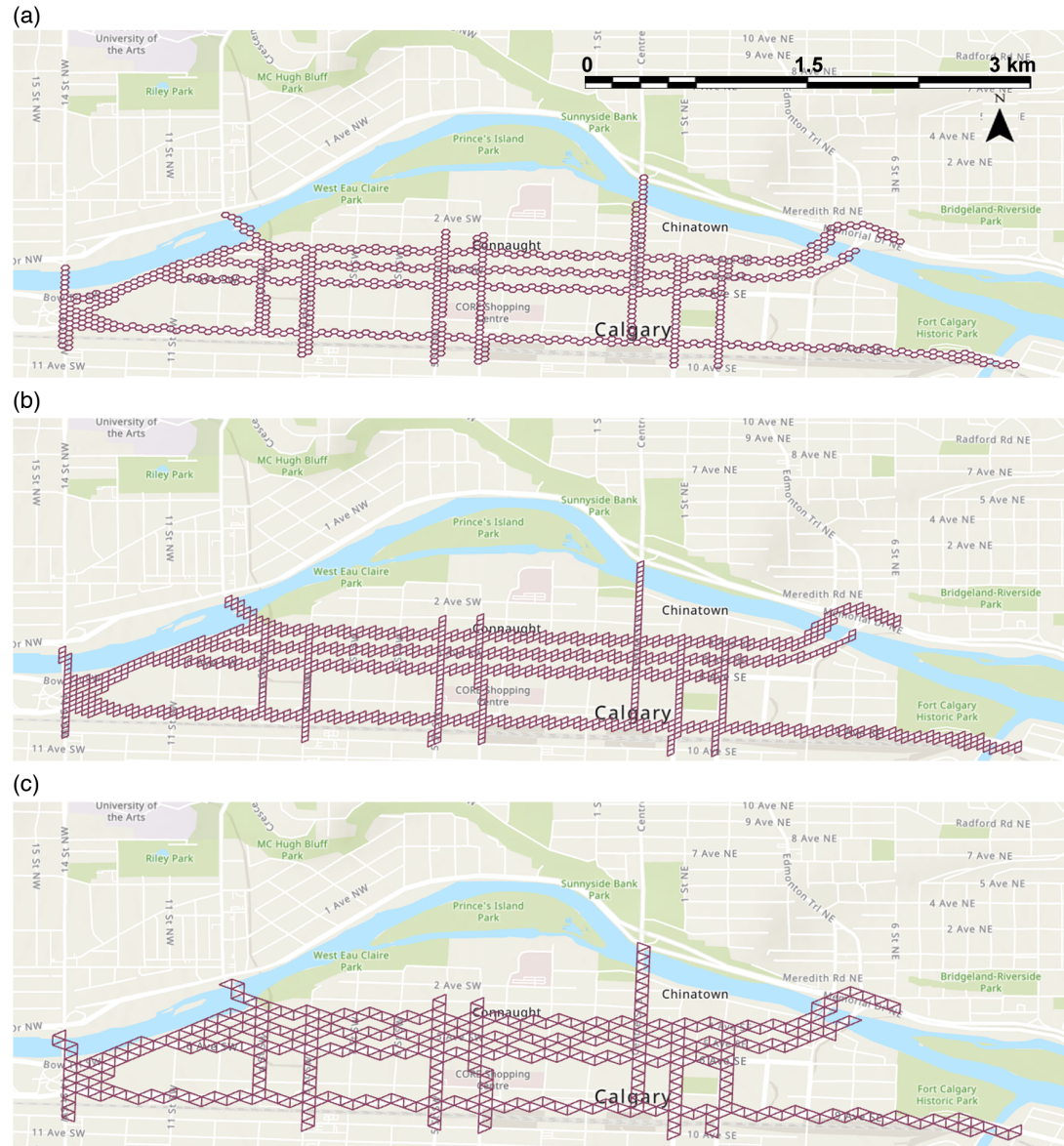


**Figure 5.** Representation of modeled line features on various tessellations: (a) hexagonal grids, (b) diamond grids, and (c) triangular grids. The grids were created via the dggridR library (Barnes 2016) and visualized in ArcGIS Pro 2.4 with the “World Topographic Map” as the base map (Esri 2020). [Colour online.]



continuous space. In this study, the calculation of the total inter-centroid distance of a modeled line feature was used to quantify the preserved fidelity of the line features. Specifically, the average delta length ( $\bar{\Delta}L$ ) was measured as the average absolute difference between the original length and the total inter-centroid distance among all the modeled streets. The average rate of distortion ( $\bar{R}_D$ ) was calculated as the mean ratio of the delta length to the original geodesic length of the line feature among all the modeled streets. Lower delta length and lower rates of distortion indicate higher preserved fidelity of the original feature. Because of the rasterization alike process, the total inter-centroid distance was greater

than the original feature length in most cases. As shown in [Table 2](#), how well the modeling process maintained the features' original geometry was affected by the grid shape, grid aperture, and resolution levels. For example, tessellations ISEA4H, ISEA4T, and ISEA4D have the same aperture which equals to four, while ISEA4H generally performed the best in preserving line features' geometry in this study, followed by ISEA4T and ISEA4D ([Table 2](#)). When modeling at the finest resolution where the spacing between the cell centroids was about 2 m, ISEA3H showed the highest fidelity preservation ( $\bar{\Delta}L = 106.8$  m;  $\bar{R}_D = 18.3\%$ ) compared with the other three DGGS configurations ( $\bar{\Delta}L = 112.8$ , 113.3, and 244.8 m, and  $\bar{R}_D = 21.1\%$ , 18.2%, and 36.1%, for ISEA4H, ISEA4T, and ISEA4D, respectively; [Table 2](#)).

[Figure 6](#) showed some possible scenarios of the geometry distortion that occurred during the modeling of line features on various DGGS tessellations. For example, 9 Street SW was north–south directed and across two adjacent “columns” of cells on ISEA3H and ISEA4H tessellations, which led to increasing the total inter-centroid distance measured on these two grid systems ([Figs. 6a](#) and [6b](#)). On the contrary, 8 Street SW segment A modeled on ISEA3H was free of this issue and had more fidelity preserved in this scenario ([Fig. 6a](#)). Additionally, when modeling 9 Street SW, diamond grids showed less geometry distortion ([Fig. 6d](#)) compared with the hexagonal or triangular grids ([Figs. 6a–6c](#)). When modeling an east–west directed line feature, however, such as 8 Avenue SW, modeling differences among grid configurations were mitigated ([Fig. 6](#)).

The 9 Street SW was used as an example to explore the influence of the line direction and the grid orientation on the line feature modeling. The original feature of 9 Street SW was clockwise rotated from  $0^\circ$  to  $345^\circ$  with a  $15^\circ$  interval and was modeled on various DGGS configurations. The absolute delta length (i.e., the difference between the original length and the total inter-centroid distance) was calculated for each of the tested grid tessellations, resolution levels, and the rotation degrees, with three options of the grid orientation relative to the Earth ([Figs. 7–9](#)). The geodesic length of the original line feature was 528.0 m.

Results showed that the absolute delta length was sensitive to the line direction, the grid tessellation, and the grid orientation. With the default grid orientation ( $\lambda = 58.2825^\circ$ ;  $\varphi = 11.2500^\circ$ ;  $\alpha = 0^\circ$ ), the line feature with a  $30^\circ$ – $45^\circ$  clockwise rotation showed high fidelity preservation when being modeled on ISEA3H, ISEA4H, and ISEA4T, and the similar magnitude of the fidelity occurred repeatedly about every  $90^\circ$  of rotation ([Figs. 7a–7c](#)). When being modeled on ISEA4D, a  $0^\circ$ – $30^\circ$  or  $180^\circ$ – $210^\circ$  clockwise rotation resulted in high fidelity preservation ([Fig. 7d](#)). Specifically, the lowest  $\bar{\Delta}L$  among the tested resolutions was 11.2 m with a  $210^\circ$  rotation, 5.7 m with a  $315^\circ$  rotation, 11.2 m with a  $45^\circ$  rotation, and 12.8 m with a  $15^\circ$  rotation, for ISEA3H, ISEA4H, ISEA4T, and ISEA4D, respectively ([Fig. 7](#)). Compared with the default grid orientation, the orientation options suggested by [Fuller and Applewhite \(1975\)](#) and [J. Zhou et al. \(2020\)](#) showed different results ([Figs. 8](#) and [9](#)). For example, a line feature with a  $60^\circ$  clockwise rotation had the lowest geometry distortion (among the resolutions,  $\bar{\Delta}L = 37.9$  m; [Fig. 9d](#)) when modeled on ISEA4D with the orientation of [J. Zhou et al. \(2020\)](#), compared with the  $\bar{\Delta}L$  of 118.9 ([Fig. 7d](#)) and 96.7 m ([Fig. 8d](#)) when modeled on ISEA4D with the orientation suggested by [Sahr et al. \(2003\)](#) and [Fuller and Applewhite \(1975\)](#). Furthermore, resolution levels had an impact on the preserved fidelity of a line feature, although the specific effect depended on the grid configuration. For instance, with the orientation suggested by [Fuller and Applewhite \(1975\)](#), the original 9 Street SW (rotation degree =  $0^\circ$ ) had the lowest geometry distortion when being modeled on ISEA4T at the finest resolution (delta length at resolution 21 = 72.9 m; [Fig. 8c](#)), while had the highest geometry distortion when being modeled on ISEA3H, ISEA4H, and ISEA4D at the finest resolution among all tested resolutions (delta length at the finest

**Table 2.** Average delta length ( $\overline{\Delta L}$ ) and rate of distortion ( $\overline{R_D}$ ) of modeled streets ( $n = 40$ ) on the grid configurations ISEA3H, ISEA4H, ISEA4T, and ISEA4D at five successive resolution levels.

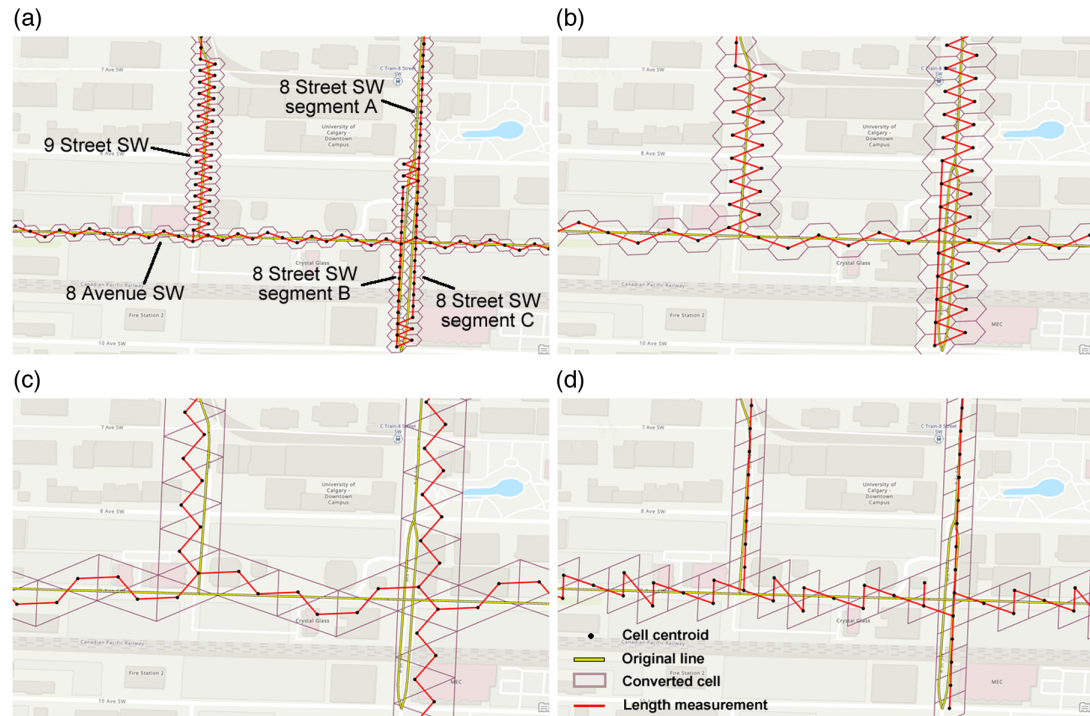
ISEA3H			ISEA4H			ISEA4T			ISEA4D		
Resolution level	$\overline{\Delta L}^a$ (m)	$\overline{R_D}^b$ (%)	Resolution level	$\overline{\Delta L}$ (m)	$\overline{R_D}$ (%)	Resolution level	$\overline{\Delta L}$ (m)	$\overline{R_D}$ (%)	Resolution level	$\overline{\Delta L}$ (m)	$\overline{R_D}$ (%)
24	94.5	17.2	18	100.1	17.7	17	125.6	27.6	18	189.7	31.0
25	109.6	19.6	19	85.0	16.7	18	124.2	22.7	19	201.0	31.2
26	87.8	14.5	20	90.2	15.5	19	123.1	21.1	20	202.7	30.9
27	109.0	18.7	21	94.9	16.8	20	125.2	20.5	21	201.2	29.7
28	106.8	18.3	22	112.8	21.1	21	113.3	18.2	22	244.8	36.1

Note: ISEA3H, Icosahedral Snyder Equal Area Aperture 3 Hexagonal Grid; ISEA4H, Icosahedral Snyder Equal Area Aperture 4 Hexagonal Grid; ISEA4T, Icosahedral Snyder Equal Area Aperture 4 Triangular Grid; ISEA4D, Icosahedral Snyder Equal Area Aperture 4 Diamond Grid.

<sup>a</sup>Average delta length is calculated as the mean absolute difference between the original length and the total inter-centroid distance among all the modeled lines.

<sup>b</sup>Average rate of distortion is calculated as the mean ratio of the delta length to the geodesic length of the original line feature among all the modeled lines.

**Figure 6.** Example of the original and modeled streets along with the length measurement in the tessellations of (a) Icosahedral Snyder Equal Area Aperture 3 Hexagonal Grid (ISEA3H) at resolution 24, (b) Icosahedral Snyder Equal Area Aperture 4 Hexagonal Grid (ISEA4H) at resolution 18, (c) Icosahedral Snyder Equal Area Aperture 4 Triangular Grid (ISEA4T) at resolution 17, and (d) Icosahedral Snyder Equal Area Aperture 4 Diamond Grid (ISEA4D) at resolution 18. The grids and cell centroids were created via the dggridR library (Barnes 2016) and visualized in ArcGIS Pro 2.4 with the “World Topographic Map” as the base map (Esri 2020). [Colour online.]



resolutions = 71.3, 88.3, and 250.1 m, on ISEA3H, ISEA4H, and ISEA4D, respectively; Figs. 8a, 8b, and 8d). Given the results of the geometry distortion when modeling line features on various DGGS configurations, a line generalization algorithm is needed to maintain the main geometry and topological constraints of the original line in the context of DGGS, especially when transmitting from a fine resolution to a coarse resolution (e.g., Stefanakis 2016).

#### Polygons

Polygons of land cover classification were modeled on different DGGS configurations (Fig. 10). Table 3 summarises the average delta area ( $\bar{\Delta S}$ ) and the rate of distortion of modeled blocks on the tessellations ISEA3H, ISEA4H, ISEA4T, and ISEA4D at five successive resolution levels, in which  $\bar{\Delta S}$  is calculated as the mean absolute difference between the original polygon area and the total DGGS cell area, and the  $\bar{R}_D$  is calculated as the mean ratio of the delta area to the geodesic area of the original polygon. Lower delta area and lower rates of distortion indicate less distortion of the original feature. When modeling at the finest resolution in which the spacing between the cell centroids was about 2 m, ISEA3H showed the least distortion ( $\bar{\Delta S} = 10.1 \text{ m}^2$ ;  $\bar{R}_D = 4.9\%$ ), followed by ISEA4H ( $\bar{\Delta S} = 17.2 \text{ m}^2$ ;  $\bar{R}_D = 6.9\%$ ), ISEA4D ( $\bar{\Delta S} = 21.4 \text{ m}^2$ ;  $\bar{R}_D = 7.1\%$ ), and ISEA4T ( $\bar{\Delta S} = 27.7 \text{ m}^2$ ;  $\bar{R}_D = 9.9\%$ ) (Table 3). For each of the tested grid tessellations, finer resolution levels corresponded to lower  $\bar{\Delta S}$  and lower  $\bar{R}_D$  (Table 3).

**Figure 7.** Measured geometry distortion of the clockwise rotated 9 Street SW when modeled on (a) Icosahedral Snyder Equal Area Aperture 3 Hexagonal Grid (ISEA3H), (b) Icosahedral Snyder Equal Area Aperture 4 Hexagonal Grid (ISEA4H), (c) Icosahedral Snyder Equal Area Aperture 4 Triangular Grid (ISEA4T), and (d) Icosahedral Snyder Equal Area Aperture 4 Diamond Grid (ISEA4D), with the discrete global grid systems orientation parameters: latitude of the pole ( $\lambda$ ) = 58.2825°, longitude of the pole ( $\varphi$ ) = 11.2500°, and azimuth ( $\alpha$ ) = 0°. [Colour online.]

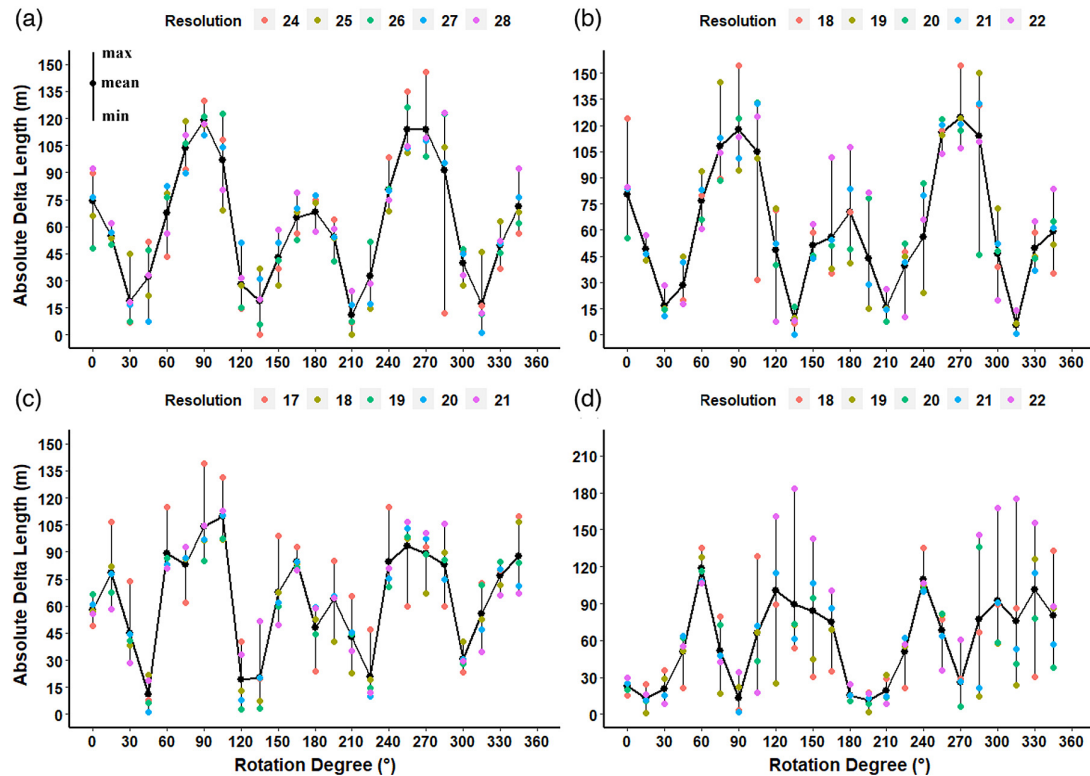
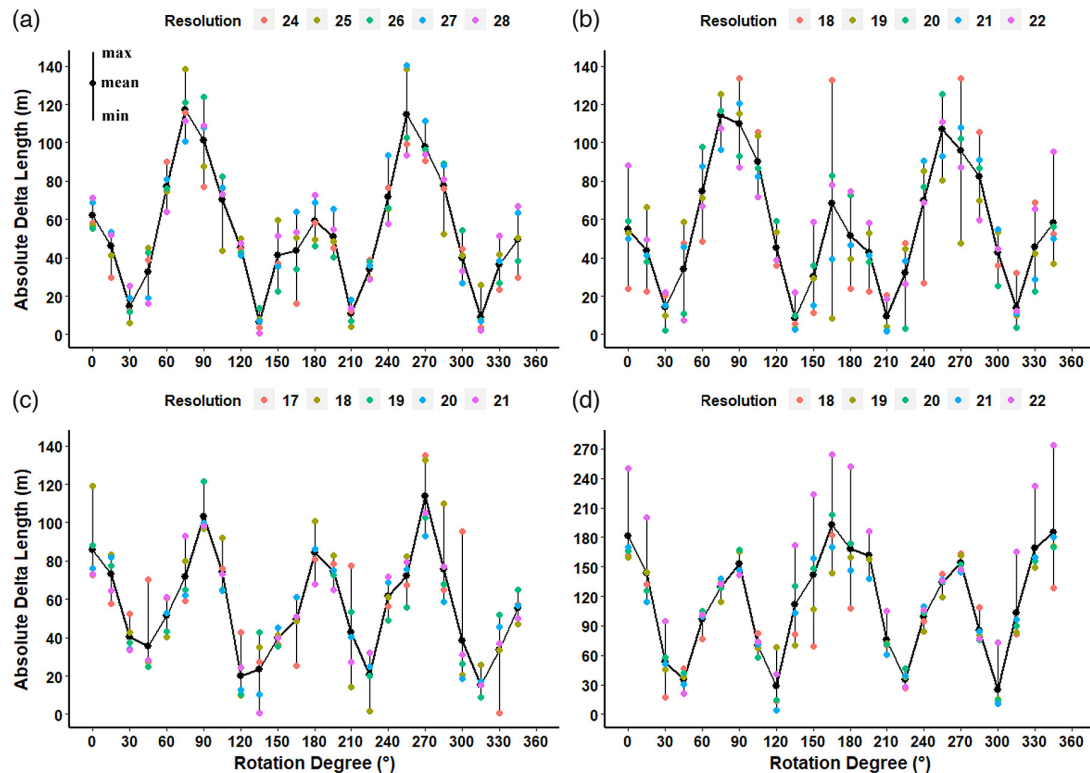


[Figure 11](#) visualized how grid tessellations and resolution levels can affect the modeling of areal objects, using the downtown campus of the University of Calgary as an example. The building has an original geodesic area of 3873.1 m<sup>2</sup> with a rectangle alike shape; it has various appearing shapes and was measured with a deviated area with different configurations and granularities. As illustrated in [Fig. 11](#), with the coarsest resolution, all four grid tessellations provided poor modeling accuracy: 3625.1 m<sup>2</sup> ( $\overline{R_D} = 6.4\%$ ), 5214.6 m<sup>2</sup> ( $\overline{R_D} = 34.6\%$ ), 2979.8 m<sup>2</sup> ( $\overline{R_D} = 23.1\%$ ), and 4469.7 m<sup>2</sup> ( $\overline{R_D} = 15.4\%$ ) of area measurement with ISEA3H at resolution 24, ISEA4H at resolution 18, ISEA4T at resolution 17, and ISEA4D at resolution 18, respectively. With the finer resolutions, the modeling accuracy was largely improved: 3860.1 m<sup>2</sup> ( $\overline{R_D} = 0.3\%$ ), 3870.2 m<sup>2</sup> ( $\overline{R_D} = 0.1\%$ ), 3893.5 m<sup>2</sup> ( $\overline{R_D} = 0.5\%$ ), and 3876.0 m<sup>2</sup> ( $\overline{R_D} = 0.1\%$ ) of area measurement with ISEA3H at resolution 28, ISEA4H at resolution 22, ISEA4T at resolution 21, and ISEA4D at resolution 22, respectively ([Fig. 11](#)). The appearing shapes also better mimicked the building's real shape at these finer resolutions ([Fig. 11](#)). Clearly, the modeling results of this building in some scenarios of coarse resolutions were not acceptable in a real application. Hence, a rule is expected to set the visibility scale range of areal objects in a DGGS specification, so that an object would be automatically omitted from a specific level and all its lower (coarser) levels. The rule can be set based on  $\overline{R_D}$ , and an areal object will be omitted, for instance, when its  $\overline{R_D} > 25\%$ .

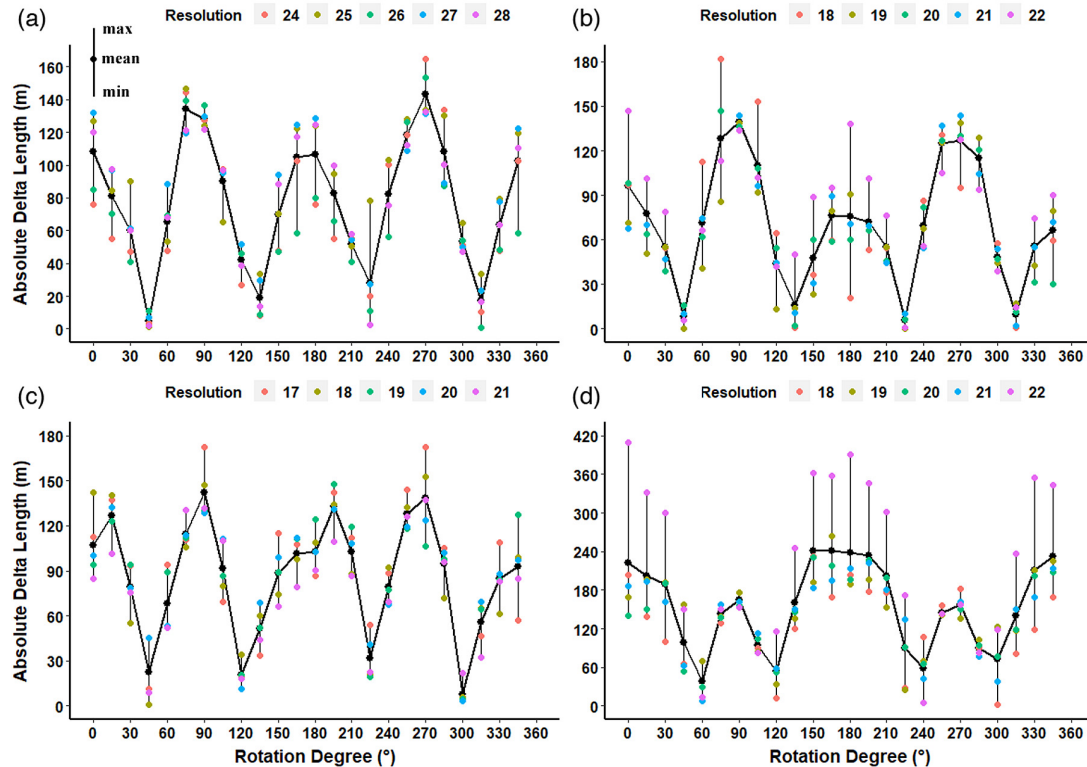
**Figure 8.** Measured geometry distortion of the clockwise rotated 9 Street SW when modeled on (a) Icosahedral Snyder Equal Area Aperture 3 Hexagonal Grid (ISEA3H), (b) Icosahedral Snyder Equal Area Aperture 4 Hexagonal Grid (ISEA4H), (c) Icosahedral Snyder Equal Area Aperture 4 Triangular Grid (ISEA4T), and (d) Icosahedral Snyder Equal Area Aperture 4 Diamond Grid (ISEA4D), with the discrete global grid systems orientation parameters: latitude of the pole ( $\lambda$ ) = 2.3009°, longitude of the pole ( $\varphi$ ) = -5.2454°, and azimuth ( $\alpha$ ) = 7.4666°. [Colour online.]



### Topological uncertainties

The topological issues between the same geometry type, including point-to-point, line-to-line, and polygon-to-polygon relationships can be generated naturally through the resolution conversion, typically from a fine resolution to a coarse resolution, in the form of generalization. Two or more point-features are possible to be generalized as one cell on a DGGS if their distance is comparable to or smaller than the cell size. In this study, traffic cameras were disjointed with each other after being modeled in all tested scenarios because the distances between the traffic cameras in downtown Calgary were far greater than the tested cell sizes. In the same manner, original line-to-line and polygon-to-polygon relationships can be violated due to the generalization at a coarse resolution. For example, as shown in Fig. 6, 8 Street SW segment B and segment C were modeled as two sets of cells sharing multiple common cells on ISEA3H resolution 24 and ISEA4H resolution 18 (i.e., more than two intersections; Figs. 6a and 6b) and were generalized as one single feature on ISEA4D resolution 18 (Fig. 6d), although these two segments should have only met at the start point and the endpoint, realistically. Figure 12 shows the modeling results of the street block constituted by 2 Avenue SE, 1 Street SE, 3 Avenue SE, and Centre Street S in downtown Calgary on all tested grid tessellation at the finest and the coarsest resolutions. Generalization processes occurred when modeling on coarse resolutions, where Building A and Building B were generalized as a single building with the attribute of

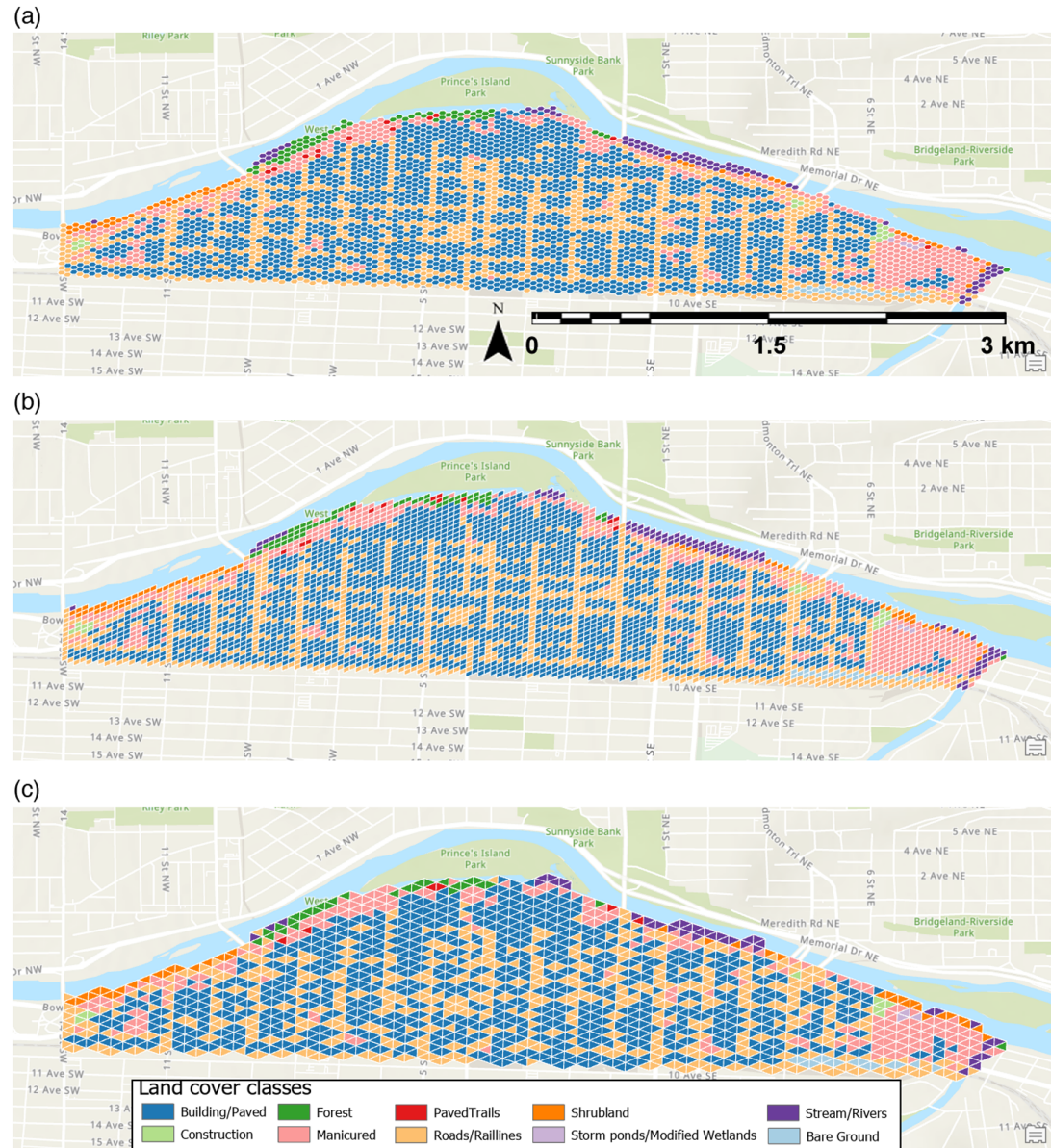
**Figure 9.** Measured geometry distortion of the clockwise rotated 9 Street SW when modeled on (a) Icosahedral Snyder Equal Area Aperture 3 Hexagonal Grid (ISEA3H), (b) Icosahedral Snyder Equal Area Aperture 4 Hexagonal Grid (ISEA4H), (c) Icosahedral Snyder Equal Area Aperture 4 Triangular Grid (ISEA4T), and (d) Icosahedral Snyder Equal Area Aperture 4 Diamond Grid (ISEA4D), with the discrete global grid systems orientation parameters: latitude of the pole ( $\lambda$ ) = 37.6895°, longitude of the pole ( $\varphi$ ) = -51.6218°, and azimuth ( $\alpha$ ) = -72.6482°. [Colour online.]



Building A on ISEA4H resolution 18 (Fig. 12b), and Building A and Building C were generalized and assigned with the attribute of Building C on ISEA4T resolution 17 (Fig. 12c) and ISEA4D resolution 18 (Fig. 12d). Because the cells were assigned with the attribute of the original polygon with the higher intersected area during the quantization process in this study, each cell was attached with only one land cover attribute. Hence, the topology rule that land cover classes should meet with the adjacent ones at boundaries was fulfilled in this study. To solve the topological distortion between the same type of geo-features (i.e., point-to-point, line-to-line, and polygon-to-polygon), L. Zhou et al. (2020) proposed to determine the topological distortion between the target spatial objects by detecting the topology at the cell level and then increasing the local resolution of the vector features. Although the generalization process is needed to accommodate cartographic entities especially when mapping at a large scale, the rules of generalization and the methods to maintain the relationships between the representational instances of the individual entities still need further exploration in the context of DGGS.

Challenges also exist regarding the topological relationships between different types of geo-features. Although all traffic cameras met streets in all tested scenarios in this study, point-to-line relationships still need consideration in a real DGGS application. For example, when applying a line simplification algorithm in the DGGS context, the spatial

**Figure 10.** Representation of modeled polygon features on various tessellations: (a) hexagonal grids, (b) diamond grids, and (c) triangular grids. The grids were created via the dggridR library (Barnes 2016) and visualized in ArcGIS Pro 2.4 with the “World Topographic Map” as the base map (Esri 2020). [Colour online.]



relationships including topology and direction between the simplified line feature and its surrounding objects are expected to be maintained. Stefanakis (2016) proposed a solution named mR-V line simplification, which was compliant with the raster tiled maps used by the common web map browsers and had the potential to be applied on DGGS. The study has shown the line simplification results by applying the mR-V algorithm to an octahedron-based DGGS (Goodchild et al. 1991). Nonetheless, the algorithm or other line generalization algorithms for DGGS are expected to be developed for various tessellations and

**Table 3.** Average delta area ( $\overline{\Delta S}$ )<sup>a</sup> and rate of distortion ( $\overline{R_D}$ )<sup>b</sup> of modeled blocks ( $n = 1122$ ) on the grid configurations ISEA3H, ISEA4H, ISEA4T, and ISEA4D at five successive resolution levels.

ISEA3H			ISEA4H			ISEA4T			ISEA4D		
Resolution level	$\overline{\Delta S}$ (m <sup>2</sup> )	$\overline{R_D}$ (%)	Resolution level	$\overline{\Delta S}$ (m <sup>2</sup> )	$\overline{R_D}$ (%)	Resolution level	$\overline{\Delta S}$ (m <sup>2</sup> )	$\overline{R_D}$ (%)	Resolution level	$\overline{\Delta S}$ (m <sup>2</sup> )	$\overline{R_D}$ (%)
24	258.9	58.5	18	542.9	83.5	17	803.9	92.6	18	576.3	84.4
25	129.6	37.4	19	263.7	62.0	18	385.7	73.7	19	292.7	63.0
26	67.8	21.2	20	112.3	32.5	19	180.7	47.4	20	133.3	36.9
27	24.9	9.8	21	43.7	15.2	20	73.1	24.8	21	53.8	17.5
28	10.1	4.9	22	17.2	6.9	21	27.7	9.9	22	21.4	7.1

Note: ISEA3H, Icosahedral Snyder Equal Area Aperture 3 Hexagonal Grid; ISEA4H, Icosahedral Snyder Equal Area Aperture 4 Hexagonal Grid; ISEA4T, Icosahedral Snyder Equal Area Aperture 4 Triangular Grid; ISEA4D, Icosahedral Snyder Equal Area Aperture 4 Diamond Grid.

<sup>a</sup>Average delta area is calculated as the mean absolute difference between the original polygon area and the total DGGS cell area.

<sup>b</sup>Average rate of distortion is calculated as the mean ratio of the delta area to the geodesic area of the original polygon.

**Figure 11.** Representation of the downtown campus of the University of Calgary on (a) Icosahedral Snyder Equal Area Aperture 3 Hexagonal Grid (ISEA3H) resolution 24/26/28, (b) Icosahedral Snyder Equal Area Aperture 4 Hexagonal Grid (ISEA4H) resolution 18/20/22, (c) Icosahedral Snyder Equal Area Aperture 4 Triangular Grid (ISEA4T) resolution 17/19/21, and (d) Icosahedral Snyder Equal Area Aperture 4 Diamond Grid (ISEA4D) resolution 18/20/22. The modeled campus building is highlighted with red boundaries with the black frame representing the original polygon. The grids were created via the dggridR library (Barnes 2016) and visualized in ArcGIS Pro 2.4. [Colour online.]

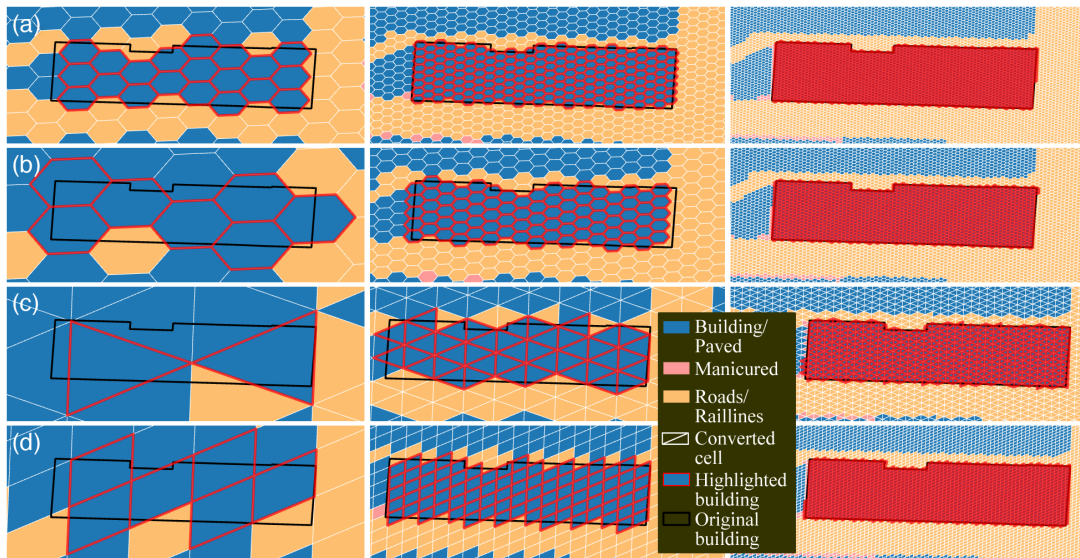
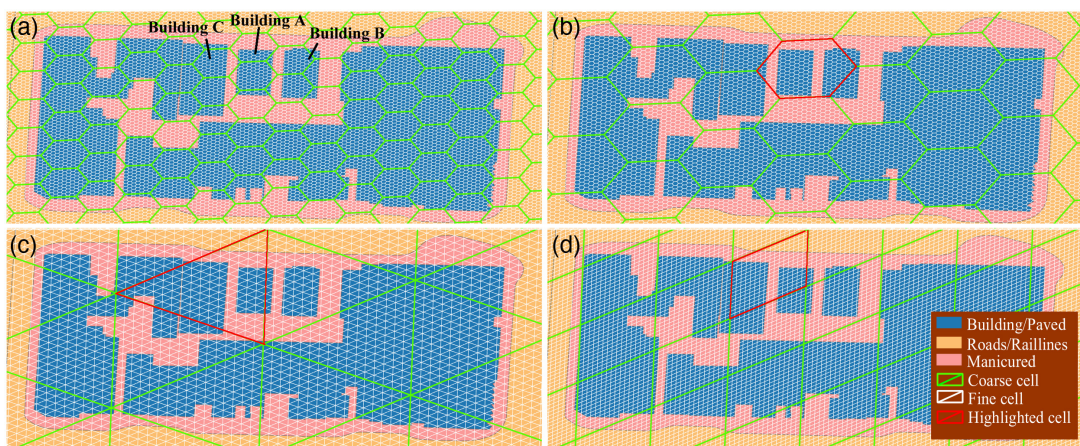


**Figure 12.** Representation of a sample street block on (a) Icosahedral Snyder Equal Area Aperture 3 Hexagonal Grid (ISEA3H) resolution 24 and 28, (b) Icosahedral Snyder Equal Area Aperture 4 Hexagonal Grid (ISEA4H) resolution 18 and 22, (c) Icosahedral Snyder Equal Area Aperture 4 Triangular Grid (ISEA4T) resolution 17 and 21, and (d) Icosahedral Snyder Equal Area Aperture 4 Diamond Grid (ISEA4D) resolution 18 and 22. Specific coarse cells are highlighted with red boundaries. The grids were created via the dggridR library (Barnes 2016) and visualized in ArcGIS Pro 2.4. [Colour online.]



tested at multiple resolutions. Besides, other topological violations found in this study included that cameras or main streets were not always inside of or covered by the “Roads/Rail lines” land cover class. Although modeling at a finer resolution contributed to fewer topological errors, a method is needed to repair the violated topology in the quantization process for DGGS applications at any resolution. Traditionally, Egenhofer’s dimensionally extended nine-intersection model (DE-9IM) was used to define relationships between two geo-features by defining their external, border, and interior areas ([Egenhofer and Herring 1990](#)). This topology description model can be adjusted and extended to work in the DGGS context. For example, Global Grid Systems employed the adjusted DE-9IM by ignoring the geometries’ border, defining the border by using DGGS cells connectivity, or defining the border by the coverage information regarding the geometry for each cell ([Peterson 2016](#); [GGS 2019](#)).

## Conclusions

This study modeled traffic cameras (points), main streets (lines), and land cover classifications (polygons) of downtown Calgary with various DGGS configurations and granularities. The uncertainties of geometry and topology of these spatial objects were analyzed and discussed.

Specifically, geometric uncertainties were quantitatively measured as the point position displacement (i.e., the distance between the geographical coordinates of the original point and the geographical coordinates of the converted cell centroid) and line and polygon features’ geometry fidelity (i.e., the difference between the original length or area and the total inter-centroid distance or cell area). Point displacement generally reduced when being modeled at a higher resolution, although the displacement can diverge when transitioning to another resolution on the tessellation ISEA4D due to the lack of the monotonical convergence characteristic. The modeled line features’ fidelity was influenced by the grid tessellation, the resolution level, the grid orientation relative to the Earth, and the rotated line directions. The degree of distortion was not straightforward to predict. A line simplification algorithm should be helpful to maintain the primary geometry and topological constraints of the original line in the context of DGGS. The modeled polygon features’ fidelity was found to be higher with finer resolution levels for all tested DGGS configurations: ISEA3H, ISEA4H, ISEA4T, and ISEA4D. To avoid the extreme distortion when modeling polygons on DGGS in a real application, a rule of visibility scale range based on the distortion rate can be set to omit an object whose distortion rate is beyond a threshold (e.g., 25%) at a specific resolution level and all its coarser levels.

Topological uncertainties were discussed in the cases of that between the same feature type and between different feature types. When transmitting from a fine resolution to a coarse resolution, a generalization of the objects with the same geometry type can occur naturally, but this can lead to topology errors in some scenarios. The rules of generalization and the methods to maintain the relationships between the representational instances of the individual entities still need further exploration in the context of DGGS. Challenges also exist in maintaining the topological relationships between different geo-feature types. In particular, during the line simplification process, the algorithm should consider the validity of the spatial relationships between the simplified line feature and its surrounding objects. A modified topological data model, such as an adjusted Egenhofer’s DE-9IM can be extended to fit in the DGGS context.

Both geometric and topological uncertainties discussed in this study should be considered when applying DGGS implementations to a specific domain. The results of this study were beneficial to DGGS user communities in terms of the selection among grid types, refinement ratios, and resolution levels. This study also suggested several research

directions that can benefit the quantization and analysis of vector features on DGGS, such as the line simplification algorithms that maintain the valid topology with the surrounding objects, the topological data model that can work for DGGS, and the generalization rules especially for the visualization of DGGS contents.

### Acknowledgements

This research has been funded by the Canadian Natural Sciences and Engineering Research Council (NSERC) Discovery Grant program entitled HALOS: Mapping Linear Features on Modern Geospatial Reference Frameworks (2019–2024).

### References

- Ahlqvist, O., Keukelaar, J., and Oukbir, K. 2000. Rough classification and accuracy assessment. *Int. J. Geogr. Inf. Sci.* **14**(5): 475–496. doi:[10.1080/13658810050057605](https://doi.org/10.1080/13658810050057605).
- Alderson, T., Purss, M., Du, X., Mahdavi-Amiri, A., and Samavati, F. 2020. Digital earth platforms. Pages 25–54 in H. Guo, M. Goodchild, and A. Annoni, eds. *Manual of digital earth*. Springer, Singapore.
- Barnes, R. 2016. dggridR: discrete global grids for R. [Online]. Available from <https://github.com/r-barnes/dggridR> [5 March 2020].
- Bondaruk, B., Roberts, S.A., and Robertson, C. 2020. Assessing the state of the art In Discrete Global Grid Systems: OGC criteria and present functionality. *Geomatica*, **74**: 9–30. doi:[10.1139/geomat-2019-0015](https://doi.org/10.1139/geomat-2019-0015).
- Bowater, D., and Stefanakis, E. 2019. An open-source web service for creating quadrilateral grids based on the rHEALPix discrete global grid system. *Int. J. Digit. Earth*, **13**: 1055–1071. doi:[10.1080/17538947.2019.1645893](https://doi.org/10.1080/17538947.2019.1645893).
- Egenhofer, M.J., and Herring, J.R. 1990. A mathematical framework for the definition of topological relations. *Proc. Fourth International Symposium on Spatial Data Handling*. pp. 803–813.
- Esri. 2020. Topographic [basemap]. World Topographic Map [information date 23 September 2020]. [Online]. Available from <https://www.arcgis.com/home/item.html?id=30e5fe3149c34df1ba922e6f5bbf808f> [5 October 2020].
- Fuller, R.B., and Applewhite, E.J. 1975. *Synergetics: explorations in the geometry of thinking*. MacMillan Publishing Co. Inc., New York, NY, USA.
- GGS. 2019. Global grid systems. [Online]. Available from <https://www.globalgridsystems.com> [20 November 2019].
- Gibb, R. 2016. The rHEALPix discrete global grid system. IOP Conference Series: Earth and Environmental Science, 9th Symposium of the International Society for Digital Earth (ISDE), Halifax, NS, Canada.
- Goodchild, M.F. 1989. Modelling error in objects and fields. Pages 107–113 in M.F. Goodchild and S. Gopal, eds. *Accuracy of spatial databases*. Taylor & Francis, Basingstoke, UK.
- Goodchild, M.F. 2018. Reimagining the history of GIS. *Ann. GIS*, **24**(1): 1–8. doi:[10.1080/19475683.2018.1424737](https://doi.org/10.1080/19475683.2018.1424737).
- Goodchild, M.F., and Yang, S. 1989. A hierarchical spatial data structure for global Geographic Information Systems. *Graph. Models Image Process.* **54**(1): 31–44. doi:[10.1016/1049-9652\(92\)90032-S](https://doi.org/10.1016/1049-9652(92)90032-S).
- Goodchild, M.F., Yang, S., and Dutton, G. 1991. Spatial data representation and basic operations for a triangular hierarchical data structure. National Center for Geographic Information and Analysis Report 91-8.
- JPL. 2018. HEALPix. [Online]. Available from <https://healpix.sourceforge.io/index.php> [20 November 2019].
- Lee, K.H., Cho, S.B., and Choy, Y.C. 2000. Automated vectorization of cartographic maps by a knowledge-based system. *Eng. Appl. Artif. Intell.* **13**(2): 165–178. doi:[10.1016/S0952-1976\(99\)00049-4](https://doi.org/10.1016/S0952-1976(99)00049-4).
- Mahdavi-Amiri, A., Bhojani, F., and Samavati, F. 2013. One-to-two digital earth. Pages 681–692 in G. Bebis, R. Boyle, B. Parvin, D. Koracin, B. Li, F. Porikli, et al., eds. *Advances in visual computing. Lecture notes in computer science. Proc. 9th International Symposium on Visual Computing*. Springer, Berlin, Germany, Rethymnon, Crete, Greece.
- Mahdavi-Amiri, A., Samavati, F., and Peterson, P. 2015a. Categorization and conversions for indexing methods of discrete global grid systems. *ISPRS Int. J. Geo-Inf.* **4**: 320–336. doi:[10.3390/ijgi4010320](https://doi.org/10.3390/ijgi4010320).
- Mahdavi-Amiri, A., Alderson, T., and Samavati, F. 2015b. A survey of digital earth. *Comput. Graph.* **53**: 95–117. doi:[10.1016/j.cag.2015.08.005](https://doi.org/10.1016/j.cag.2015.08.005).
- Mahdavi-Amiri, A., Harrison, E., and Samavati, F. 2016. Hierarchical grid conversion. *Comput.-Aided Des.* **79**: 12–26. doi:[10.1016/j.cad.2016.04.005](https://doi.org/10.1016/j.cad.2016.04.005).
- Mahdavi-Amiri, A., Alderson, T., and Samavati, F. 2018. Geospatial data organization methods with emphasis on aperture 3 hexagonal discrete global grid systems. *Cartographica*, **54**(1): 30–50. doi:[10.3138/cart.54.1.2018-0010](https://doi.org/10.3138/cart.54.1.2018-0010).
- Mocnik, F.-B. 2018. A novel identifier scheme for the ISEA aperture 3 hexagon discrete global grid system. *CaGIS*, **46**(3): 277–291. doi:[10.1080/15230406.2018.1455157](https://doi.org/10.1080/15230406.2018.1455157).
- Mocnik, F.-B. 2019. geogrid. [Online]. Available from <https://github.com/giscience/geogrid> [5 March 2020].
- OGC. 2017. Topic 21: discrete global grid system abstract specification. [Online]. Available from <http://www.opengis.net/doc/AS/dggs/1.0> [15 November 2019].
- OpenCalgary. 2020. Open Calgary: the city of Calgary's open data portal. [Online]. Available from <https://data.calgary.ca/> [5 March 2020].
- OpenEAGGR. 2017. Open equal area global GRid. [Online]. Available from <https://github.com/riskaware-ltd/open-eaggr> [26 November 2019].
- Peterson, P. 2016. Discrete global grid systems. Pages 1–10 in D. Richardson, N. Castree, M.F. Goodchild, A. Kobayashi, W. Liu, and R.A. Marston, eds. *The international encyclopedia of geography*. John Wiley & Sons, Ltd., Chichester, UK.

- R Core Team. 2020. R: a language and environment for statistical computing. R Core Team, Vienna, Austria.
- Roberts, S.A., and Robertson, C.J. 2016. Geographic information systems and science: a concise handbook of spatial data handling, representation, and computation. Oxford University Press, Oxford, UK.
- Sahr, K. 2020. DGGRID version 7.05. [Online]. Available from <https://github.com/sahrk/DGGRID> [12 March 2020].
- Sahr, K., White, D., and Kimerling, A.J. 2003. Geodesic discrete global grid systems. *CaGIS*, **30**(2): 121–134. doi:[10.1559/152304003100011090](https://doi.org/10.1559/152304003100011090).
- Sahr, K., Dumas, M., and Choudhuri, N. 2015. The PlanetRisk discrete global grid system. [Online]. Available from <https://webpages.sou.edu/~sahrk/docs/PlanetRiskDGGS.pdf> [12 November 2019].
- Stefanakis, E. 2016. MR-V: line simplification through mnemonic rasterization. *Geomatica*, **70**(4): 269–282. doi:[10.5623/cig2016-401](https://doi.org/10.5623/cig2016-401).
- Stough, T., Braverman, A., Cressie, N., Kang, E., Michalak, A.M., Nguyen, H., and Sahr, K. 2014. Visualizing massive spatial datasets using multiresolution global grids. National Institute for Applied Statistics Research Australia, University of Wollongong, Wollongong, Australia.
- Tong, X., Cheng, C., Wang, R., Ding, L., Zhang, Y., Lai, G., et al. 2019. An efficient integer coding index algorithm for multi-scale time information management. *Data Knowl. Eng.* **119**: 123–138. doi:[10.1016/j.datak.2019.01.003](https://doi.org/10.1016/j.datak.2019.01.003).
- Uber. 2017. H3: a hexagonal hierarchical geospatial indexing system. [Online]. Available from <https://github.com/uber/h3> [25 November 2019].
- Uher, V., Gajdoš, P., Snášel, V., Lai, Y.-C., and Radecký, M. 2019. Hierarchical hexagonal clustering and indexing. *Symmetry*, **11**(6): 731. doi:[10.3390/sym11060731](https://doi.org/10.3390/sym11060731).
- Wang, Y., Chen, Z., Cheng, L., Li, M., and Wang, J. 2013. Parallel scanline algorithm for rapid rasterization of vector geographic data. *Comput. Geosci.* **59**: 31–40. doi:[10.1016/j.cageo.2013.05.005](https://doi.org/10.1016/j.cageo.2013.05.005).
- Zhang, J., and Goodchild, M.F. 2002. Geographical information and uncertainty. Pages 1–7 in *Uncertainty in geographical information*. Taylor & Francis Group.
- Zhou, J., Ben, J., Wang, R., Zheng, M., Yao, X., and Du, L. 2020. A novel method of determining the optimal polyhedral orientation for discrete global grid systems applicable to regional-scale areas of interest. *Int. J. Digit. Earth*, 1–17. doi:[10.1080/17538947.2020.1748127](https://doi.org/10.1080/17538947.2020.1748127).
- Zhou, L., Lian, W., Zhang, Y., and Lin, B. 2020. A topology preserving gridding method for vector features in discrete global grid systems. *ISPRS Int. J. Geo-Inf.* **9**(3): 168. doi:[10.3390/ijgi9030168](https://doi.org/10.3390/ijgi9030168).